

# RSC Advances

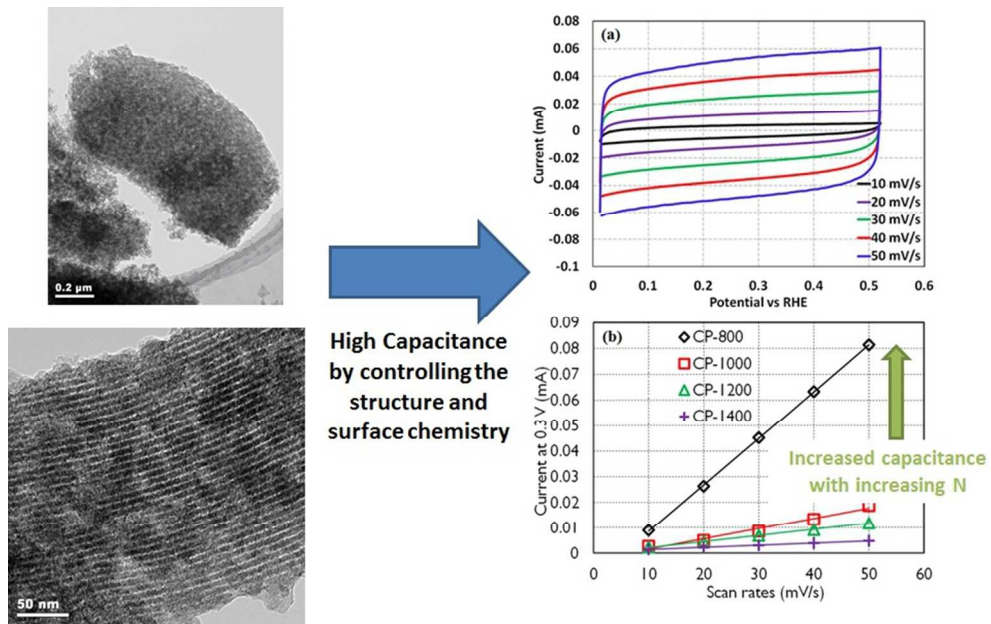


This is an *Accepted Manuscript*, which has been through the Royal Society of Chemistry peer review process and has been accepted for publication.

*Accepted Manuscripts* are published online shortly after acceptance, before technical editing, formatting and proof reading. Using this free service, authors can make their results available to the community, in citable form, before we publish the edited article. This *Accepted Manuscript* will be replaced by the edited, formatted and paginated article as soon as this is available.

You can find more information about *Accepted Manuscripts* in the [Information for Authors](#).

Please note that technical editing may introduce minor changes to the text and/or graphics, which may alter content. The journal's standard [Terms & Conditions](#) and the [Ethical guidelines](#) still apply. In no event shall the Royal Society of Chemistry be held responsible for any errors or omissions in this *Accepted Manuscript* or any consequences arising from the use of any information it contains.



256x158mm (96 x 96 DPI)

## ARTICLE

# Effect of Surface Chemistry on the Double Layer Capacitance of Polypyrrole-Derived Ordered Mesoporous Carbon

Cite this: DOI: 10.1039/x0xx00000x

Received 00th January 2012,

Accepted 00th January 2012

DOI: 10.1039/x0xx00000x

www.rsc.org/

Sujan Shrestha, Nicholas Morse, and William E. Mustain\*

In this work, the effect of nitrogen on the double layer (DL) capacitance of nitrogen-doped ordered mesoporous carbon (NOMC) is studied. The nitrogen content of the NOMCs was controlled thermally. X-ray photoelectron spectroscopy shows decreasing nitrogen content with increasing heat treatment temperature. Despite the differing N content of the NOMCs, the BET surface area, pores size and distribution of the NOMCs did not change significantly with the heat treatment, though Raman spectroscopy and X-ray diffraction showed that the microcrystallinity is affected, exposing more of the basal planes with increased heat treatment temperature. The DL capacitance of the NOMCs was measured from cyclic voltammograms in a range that minimized the contribution of the space charge capacitance and pseudocapacitance, yielding information about the impact of oxygen and nitrogen functional groups on the pure Helmholtz behavior of NOMCs. It was found that nitrogen affects the DL capacitance by changing both the electronic properties and microstructure of the carbon. These enhancements resulted in NOMCs with very high areal Helmholtz capacitance of 25.1  $\mu\text{F}/\text{cm}^2$ .

## Introduction

Natural sources of energy such as solar and wind power are inherently intermittent. Hence, there is a significant need to develop energy storage options that have high energy density, rapid charge/discharge capability and high efficiency. Electrochemical capacitors (ECs), also called supercapacitors or ultracapacitors, are one of the most promising technologies to meet this need. Though their energy density is lower than that of batteries, they can be used to complement or replace batteries in many applications because of their significantly larger power density. They are also uniquely suited for use in load levelling and uninterruptible power supply applications. Two types of ECs exist: electrochemical double layer capacitors (EDLCs) that only utilize the well-known Helmholtz storage mechanism, and redox or pseudocapacitors that are able to store charge through surface-specific redox reactions in addition to Helmholtz capacitance. EDLCs are inherently more stable compared to pseudocapacitors due to their nonfaradaic charge storage mechanism [1-2].

Carbon is the most widely used and studied material for EDLCs due to its high surface area, high conductivity, tunable porosity, electrochemical stability and low cost. Activated carbons, with porosity controlled through selective oxidation, are the most popular carbons for use in EDLCs. During activation, oxygen functional groups are formed that enhance capacitance and improve the

wettability of the carbon, but they also decrease the electronic conductivity of carbon and expedite carbon corrosion. Oxygen functional groups are also responsible for the mild pseudocapacitive behavior of carbon, primarily through the quinone/hydroquinone redox couple [3].

Recent years have seen a more complex approach to the design and synthesis of EDLC materials that simultaneously control the pore structure and surface composition. Though extensively microporous carbons have very large surface area, the rate of ion transport in microporous (pores < 2 nm) carbon is slow, which is detrimental to performance at high charge and discharge rate [4]. Mesoporous carbons (pores 2 to 50 nm) are advantageous as they can provide both fast ion transport and high surface area. Carbons with hierarchical meso/micro pores have been synthesized showing both high capacitance and good rate capability [5-6].

Nitrogen functional groups have also been introduced into EDLC active layers. Nitrogen is an interesting counter atom to oxygen. While oxygen-containing groups are generally acidic (electron withdrawing), nitrogen groups are mostly alkaline (electron donating), suggesting that they will be more stable and interact differently with the electrolyte [7]. The most successful integration of N-containing groups into EDLCs has occurred through the introduction of conducting polymers such as polyaniline and polypyrrole [8]. In some cases, the polymers have been applied

directly into composite structures with carbon [9-13]. Others have carburized the composites or the polymer directly [8, 14-15].

The resulting Nitrogen-containing carbons have been shown to be corrosion resistant [16-19]. Many studies have shown that the carbons synthesized using various nitrogen containing precursors have enhanced capacitance [20-21]. Several hypotheses have been put forward to explain the enhancement due to nitrogen doping, such as redox reactions involving nitrogen functional groups [22-23], an increase in wettability and enhancement in electronic structure of space charge layer [24-25]. Hence, the effect of nitrogen doping is still not resolved in the literature. Moreover, studying relationship between surface phenomenon and capacitance is challenging in bulk carbon because of its complex pore structure. Nitrogen also causes microstructural modification; carbons made with nitrogen precursors have more defects than the carbons made with non-nitrogen precursors [17, 26]. However, to date, a fundamental understanding that deconvolutes the effects of nitrogen surface functional groups and the carbon microstructure on the Helmholtz DL capacitance has been lacking.

Therefore, the objective of this work is to isolate and elucidate the effect of the nitrogen heteroatom on the Helmholtz DL capacitance of carbon. The nitrogen content was varied between 0 and 8.2 atomic % by heating nitrogen-doped carbon to different temperatures. The change in microstructure in terms of defects or graphiticity with the nitrogen content was characterized. To allow for precise control over surface area and pore structure, this study focused on ordered mesoporous carbon (OMC) synthesized from a SBA-15 template. Since the carbon surface area and pore structure largely depends on the template, the surface area and pore structure of the carbon was set by controlling the template structure.

## Experimental

### Synthesis of Nitrogen Functionalized Ordered Mesoporous Carbons

SBA-15 template was synthesized using a surfactant based self-assembly method [27-29]. 6.0 g of Pluronic® P 123 (BASF) was dissolved in a solution of 180 mL of 2 M HCl and 45 mL of H<sub>2</sub>O. 13.6 mL of tetraethyl orthosilicate (98 %, Acros Organics) was added to the mixture and the reaction was carried out for 20 h at 45 °C and then for 24 h at 150 °C. The solid SBA-15 precipitate was filtered and washed with copious amounts of acetone and DI water. Finally, SBA-15 was calcined at 500 °C for 3 h.

Nitrogen functionalized ordered mesoporous carbon (NOMC) was prepared by a wet pyrrole impregnation and pyrolysis procedure reported previously [30-31]. In short, 9 mL of pyrrole (Py) (C<sub>4</sub>H<sub>5</sub>N, 99 % Acros Organics) was mixed with 3.0 g of the SBA-15 template. The mixture was treated in vacuum for 24 h to improve Py infiltration into SBA-15 by capillary action. The impregnated Py was polymerized to polypyrrole (PPy) in 0.25 M FeCl<sub>3</sub> for 24 h. The composite of SBA-15 and PPy was pyrolyzed at 800 °C for 3 h in N<sub>2</sub> atmosphere. The heating rate from room temperature (RT) to 800 °C was 3 °C/min. The template was then removed with 10 M KOH at 100 °C. The resulting NOMC was washed with DI water until the

pH of the filtrate was neutral. The NOMCs were then reheated without the template at 800, 1000, 1200 or 1400 °C for 3 h. The heating rate was 3 °C/min from RT to 800 °C and 1.5 °C/min from 800 °C to the target temperature. The NOMCs are denoted as CP-X, where X represents the final heating temperature.

N-free ordered mesoporous carbon (OMC) was prepared as a 0% N control with identical pore structure to the NOMC through a similar procedure to that above with sucrose replacing Py as the template infiltrant [32]. A stock solution was made by dissolving 7.5 g of sucrose (Certified ACS, Fisher) in 30 mL of DI water. 7.5 mL of the stock solution was mixed with 2.0 g of SBA-15. The mixture was heated at 100 °C for 6 h after addition of 20 drops of sulfuric acid (NF/FCC, Fisher) to dehydrate the sucrose. To improve pore filling of the template, an additional 5 mL of the stock solution was added to the SBA-15/dehydrated sucrose. The composite was mixed with 3-5 drops of sulfuric acid and heated at 160 °C for 6 h. The SBA-15/sucrose was carburized at 900 °C for 3 h. The heating rate was 3 °C/min. The template was again removed in hot KOH. The N-free OMC is referred to as CS-900 in this work.

### Physical Characterization

The pore structure of the templated carbons was determined from their N<sub>2</sub> adsorption isotherm, which was obtained at 77 K in a Micromeritics ASAP 2020 system. Before the isotherms were collected, samples were degassed at 300 °C for 3 h in vacuum. The Brunauer-Emmett-Teller (BET) specific surface area (S<sub>BET</sub>) was calculated from the amount of N<sub>2</sub> adsorbed between relative pressures (P/P<sub>0</sub>) of 0.04 and 0.2 [33]. The total pore volume (V<sub>tot</sub>) was measured at relative pressure 0.99. To determine the pore size distribution (PSD), the Barrett-Joyner-Halenda method with Kruk-Jaroniec-Sayari correction [34], built into the ASAP 2020 V3.04 operating software, was employed.

Raman spectra were recorded with a Renishaw 2000 Spectrometer Ramascope operated by WiRE 2.0 Raman software. The laser source was a 514 nm Argon ion laser and the spectra were collected with an 1800 l/mm grating. Before every measurement, the instrument was calibrated with respect to the Si (100) peak at 521 cm<sup>-1</sup>. Peak fitting was performed using mixed Gaussian and Lorentzian functions.

X-ray diffraction (XRD) patterns were collected on a θ-2θ Bruker D8 Advance Diffractometer System with Cu anode and Ni filter from 5° to 90° with a scan rate of 0.4 °/min. The collected spectra were corrected for Kα<sub>2</sub> using Rachinger method built into DIFFRAC<sup>plus</sup> EVA software. The crystallite size was calculated from the Scherrer equation [35]:

$$t = \frac{0.9\lambda}{w \cos \theta} \quad (1)$$

where  $w$  is full width at half maximum (FWHM) at  $2\theta$  and  $\lambda$  (0.15406 nm) is the X-ray wavelength.

X-ray photoelectron spectroscopy (XPS) was used to investigate the surface composition of the carbon samples. XPS spectra were collected with a PHI Multiprobe System using unmonochromatised Al Kα radiation (1486.6 eV) operating at 250 W and 15 kV. The pressure in the analysis chamber was

$\sim 10^{-9}$  torr. Full survey spectra were taken at 100 eV pass energy with a scan rate of 1 eV/s.

### Electrochemical Characterization

Electrochemical measurements were performed in 0.5 M H<sub>2</sub>SO<sub>4</sub> at room temperature (25 °C) in a custom-built (Adams & Chittenden), three-compartment electrochemical cell with a Luggin capillary. The counter electrode (CE) was a Pt flag and the reference electrode (RE) was a K<sub>2</sub>SO<sub>4</sub> saturated Hg/Hg<sub>2</sub>SO<sub>4</sub> electrode. The electrochemical measurements were carried out with an Autolab PGSTAT302N potentiostat. Prior to each experiment, the reference electrode was calibrated against a hydrogen reference electrode (eDAQ Inc, Hydroflex) in N<sub>2</sub> (UHP, Airgas) saturated electrolyte. The data are reported with respect to the reversible hydrogen electrode (RHE).

Approximately 10.0 mg of the carbon was dispersed in a mixture of 21 mL deionized (DI) water (18 MΩ, Millipore), 4 mL isopropanol and 100 μL of 5-6 % Nafion® DE-520 dispersion (DuPont) by ultrasonication for 1 h. After ultrasonication, 30 μL of the carbon ink was pipetted onto a 0.05 μm polished glassy carbon disk electrode (Pine Instruments). The carbon ink was dried in air by rotating at 500 RPM for 1 h. The carbon loading was ca. 47 μg/cm<sup>2</sup>. Finally, the electrode was stabilized by scanning the electrode potential between 0.05 to 1.4 V at 200 mV/s for 40 cycles.

## Results and Discussion

### Pore Characteristics

The pore structure of SBA-15 has been well characterized [36]. It has a honeycomb-like pore structure with 2D hexagonal *p6mm* symmetry. It also has secondary pores located in its walls. When carbon is cast in SBA-15, the carbon structure does not collapse; the carbon nanorods formed in the primary pores are held together by carbon spacers formed in the secondary pores. Therefore, the carbon is an exact inverse replica of the template with the same *p6mm* symmetry. However, depending on the carbon precursor, infiltration of the SBA-15 pores could be incomplete, leading to a wide pore size distribution (PSD) [37-38].

The PSDs for the SBA-15 template and the resulting carbons are shown in Figure 1. The SBA-15 template showed a narrow single peak centered at 10 nm. The CP-X samples showed a narrow peak centered at 3.9 nm; however, they also had a small shoulder peak indicating an extended PSD, most likely due to slightly incomplete pore filling. The walls of the SBA-15 are populated with hydrophilic hydroxyl groups, which likely inhibits hydrophobic Py from completely filling the SBA-15 pores. CS-900 showed a single narrow peak centered at 3.9 nm, confirming that its underlying structure was the same as the NOMC.

The pore size, BET surface area ( $S_{\text{BET}}$ ) and total pore volume ( $V_{\text{tot}}$ ) for all of the CP-X carbons are summarized in Table 1.  $S_{\text{BET}}$  and  $V_{\text{tot}}$  of CP-1000 to CP-1400 were similar; ca. 593 m<sup>2</sup>/g and ca. 0.78 cm<sup>3</sup>/g. CPPy-800 had slightly higher  $S_{\text{BET}}$  (622 m<sup>2</sup>/g) and  $V_{\text{tot}}$  (0.80 cm<sup>3</sup>/g). The decrease of  $S_{\text{BET}}$  and  $V_{\text{tot}}$  were expected as some micropores collapse at higher temperatures [39]. However, the differences in  $S_{\text{BET}}$  and  $V_{\text{tot}}$  among the NOMCs were less than 5 %.

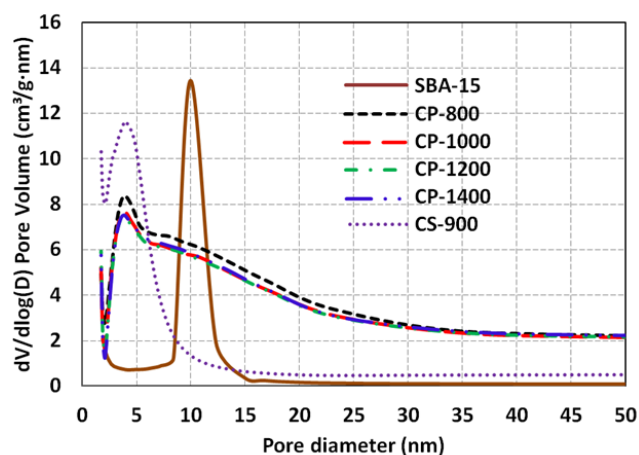


**Figure 1.** Pore size distribution curves of the SBA-15 template, CP-X carbons and CS-900.

### Surface Microstructure – Raman Spectroscopy

Raman spectra of the CP-X carbons, showing both the G and D peaks, are presented in Figure 2. The origin of the G peak is the sp<sup>2</sup> graphitic structure and has a main first order band at 1582 cm<sup>-1</sup> on pure crystalline graphite [40-41]. The D peak is rooted in disordered sp<sup>3</sup>-type carbon and has a main first order band at 1332 cm<sup>-1</sup> on a pure crystalline diamond. Hence, the presence of G and D peaks suggest that the microstructure is comprised of both crystalline and amorphous carbon structures. From the ratio of the intensity of the G and D peaks, the basal plane size of the carbon crystallites,  $L_a$ , can be calculated [42]. A third peak, commonly referred to as the A peak, representative of an amorphous graphitic phase, was added to obtain a precise fit [43]. The positions of G, D and A peaks, and  $L_a$  are reported in Table 2.

As the carbonization temperature increased, the G and D peaks of the NOMCs were better articulated. The separation between G and D peaks also increased with temperature, which can be caused by the removal of defects with increased graphiticity [44]. Another indicator of increasing graphiticity and decreasing defect density with temperature was  $L_a$ , which increased with the heat treatment temperature. Hence, at higher temperature, the average size of basal plane of carbon crystallites increased.

**Table 1.** Pore diameter, BET surface area ( $S_{\text{BET}}$ ) and pore volume ( $V_{\text{tot}}$ ) of the SBA-15 template, the nitrogen-doped carbons heated at different temperatures (CP-X), where X represents temperature.

Sample	Pore Diameter (nm)	BET Surface Area (m <sup>2</sup> /g)	Pore Volume (cm <sup>3</sup> /g)
SBA-15	10	815	1.15
CP-800	3.9	622	0.808
CP-1000	3.9	591	0.778
CP-1200	3.6	591	0.773
CP-1400	3.9	594	0.791

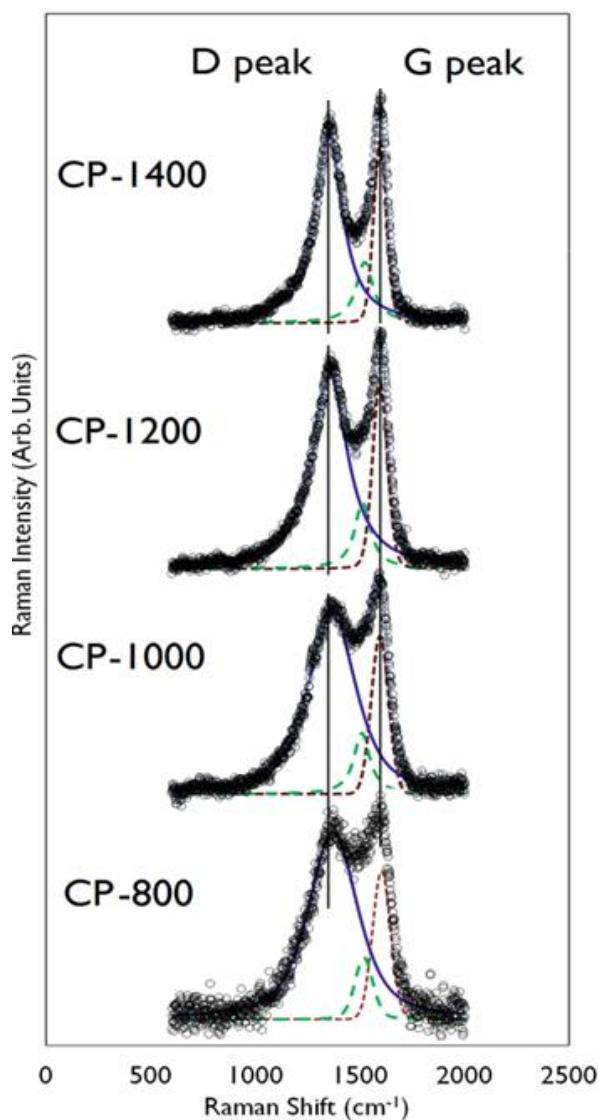


Figure 2. Raman spectra of the CP-X carbons showing D and G peaks.

### Surface Microstructure – XRD

XRD patterns for the CP-X carbons are shown in Figure 3. Several peaks representing the (102), (004), (103), (110), (112), and (006) reflections in the XRD spectra of graphitized carbon were expectedly missing [45]. This confirmed the partially amorphous nature of the carbons observed by Raman. Like the Raman spectra, the XRD peaks of the NOMCs became better defined at higher temperatures, which implied that the degree of crystallinity increased as the temperature increased. The (002) peak positions were used to calculate the d-spacing of the NOMCs (distance between graphene planes in a carbon crystallite) from Bragg's law, which are presented in Table 3. The average d-spacing of the CP-X carbons was ca. 3.59 Å, which was larger than 3.35 Å of graphite [39] suggesting turbostratic nature; i.e. lack of alignment between graphitic planes. It also showed that the heating temperature was not high enough to obtain a full graphitization.

Table 2. Peak positions of G, D and A peaks obtained after fitting Raman peaks of the nitrogen-doped carbons heated at different temperatures (CP-X).  $D_{G-D}$  is the distance between the G and D peaks.  $L_a$  is the average size of the basal planes of the carbon crystallites.

Sample	G Peak (cm <sup>-1</sup> )	A Peak (cm <sup>-1</sup> )	D Peak (cm <sup>-1</sup> )	$L_a$ (nm)	$D_{G-D}$ (cm <sup>-1</sup> )
CP-800	1604	1520	1373	3.5	231
CP-1000	1597	1510	1367	3.8	230
CP-1200	1597	1514	1358	4.2	239
CP-1400	1598	1524	1352	4.2	245

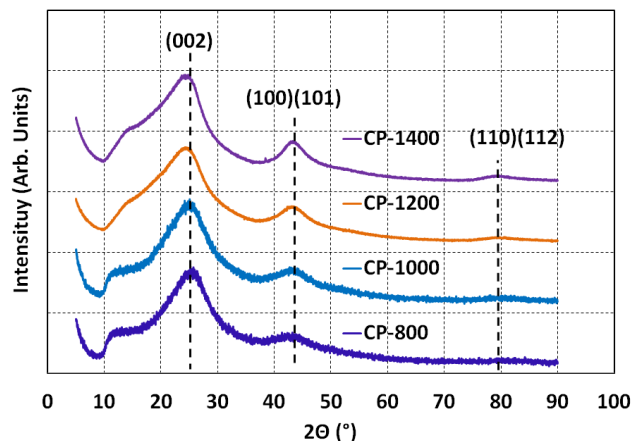


Figure 3. XRD patterns for of the CP-X carbons.

### Surface Chemistry

As shown above, the porosity among the NOMCs was quite similar; however, XPS showed significant changes in surface composition. A complete discussion of the types of functional groups for this family of materials can be found in our previous work [19]. The atomic (at) % of C, N and O were determined from C 1s, N 1s and O 1s peaks of full survey spectra and are summarized in Table 4. The nitrogen content decreased from 8.2 at % (800 °C) to 0.5 at % (1400 °C) while the oxygen content decreased from 6.2 at % (800 °C) to 3.1 at % (1400 °C). In fact, at 1400 °C, the nitrogen content was within the error limit of XPS (< 1 %). The lessening in the number of heteroatoms was expected, since at high temperatures the carbon surface undergoes surface reconstruction to increase graphiticity. For example, there is an increase in the sp<sup>2</sup> hybridized carbon atoms on the graphene plane by “smoothing” the surface and removing surface defects. The increase in the degree of graphitization at higher temperatures was supported by Raman and XRD. In addition, because oxygen is more reactive than nitrogen, oxygen was more prevalent than N at high temperatures.

### Electrochemical Properties – Effect of Potential

Cyclic voltammograms (CVs) with increasing threshold potentials were collected at a scan rate of 10 mV/s, which are

**Table 3.** Peak position ( $2\theta$ ) and FWHM of the (002) reflection of the carbon samples obtained from the XRD spectra. Carbon d-spacing and the average stack height of the carbon crystallites ( $L_c$ ) were calculated using  $2\theta$  and FWHM of the (002) reflection.

Sample	$2\theta$ (002)	Carbon d-spacing (Å)	FWHM (002)	$L_c$ (nm)
CP-800	25.7	3.46	5.18	1.57
CP-1000	24.2	3.68	5.41	1.50
CP-1200	24.6	3.62	5.37	1.51
CP-1400	24.8	3.59	4.79	1.70

**Table 4.** The gravimetric capacitance ( $C_M$ ) and areal capacitance ( $C_A$ ) of the carbon samples obtained from the slopes of the lines in Figure 6b. The oxygen content, nitrogen content and total heteroatom content were obtained from the full survey of the XPS spectra of carbon samples

Sample	$C_M$ (F/g)	$C_A$ ( $\mu\text{F}/\text{cm}^2$ )	O (at %)	N (at %)	O+N (at %)
CP-800	156.0	25.1	6.2	8.2	14.4
CP-1000	35.2	6.0	5.8	3.5	9.3
CP-1200	20.5	3.5	3.7	1.3	5.0
CP-1400	7.1	1.2	3.1	0.5	3.6

shown in Figure 4 for CP-800. The behavior depicted in Figure 4A was typical for all of the NOMCs. As seen in Figure 4, as the upper potential limit was increased, the magnitude of the negative current increased while the magnitude of the positive current remained constant. This behavior is typical of carbon materials and is a result of the quinone/hydroquinone redox couple [46]. An interesting observation was that CVs with upper potential thresholds above 0.5 V did not show a well defined quinone peak despite the high oxygen content (6.2 at % for CP-800), though these peaks were visible for CS-900. The peak suppression may stem from interaction of oxygen and nitrogen functional groups or the formation of pyridine N-oxides and  $\text{NO}_x$ .

The data shown in Figure 4 contains three contributions to the observed capacitance: Helmholtz DL capacitance, which is our focus here, space charge capacitance and pseudocapacitance. Even if the experimental data were reduced in size to eliminate the contribution of the pseudocapacitance, bound by (0.0V, 0.6V), the observed response,  $C$ , would still contain the space charge,  $C_{SC}$ , and Helmholtz,  $C_H$ , contributions, related by Equation 2.

$$\frac{1}{C} = \frac{1}{C_{SC}} + \frac{1}{C_H} \quad (2)$$

The observed capacitance has a well known parabolic relationship with electrode potential. The minima is typically observed around the potential of zero charge (PZC) [39]. Though it is well known that the PZC is a function of the N content; the minima is not always

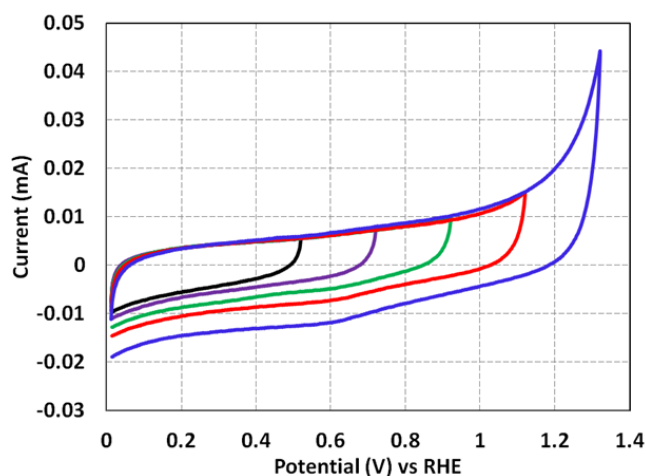


**Figure 4.** Cyclic voltammograms of CP-800 with increasing upper potential limits at a scan rate of 10 mV/s in  $\text{N}_2$ -saturated 0.5 M  $\text{H}_2\text{SO}_4$  at 25 °C.

shifted at low to moderate N-doped (~4-8%) carbon [26] due to complexities in the shift of the Fermi level with increasing N content and its balance with structural and other electronic effects. The potential where the minimum capacitance is observed is an electrochemically important one; it represents the point where contribution of the space charge capacitance to the observed behavior is its lowest. Therefore, if the minima can be found for all of the NOMCs, the resulting data can be compared to give trends in the Helmholtz capacitance as a function of N content.

The potential dependence for the observed capacitance for all of the NOMCs is shown in Figure 5. Akin to graphitic carbon, a parabolic relationship was observed for all of the samples. In each case, the data was fit by with a second degree polynomial. The minima were found from the first derivative,  $\partial C/\partial E=0$ , and the curvature of each plot was calculated from the second derivative,  $\partial^2 C/\partial E^2 = \text{constant}$ , of the polynomial functions. Surprisingly, the minima for all of these plots was nearly 0.3 V. Also, it was observed that the CVs were always symmetrical at ~0.3V when the threshold

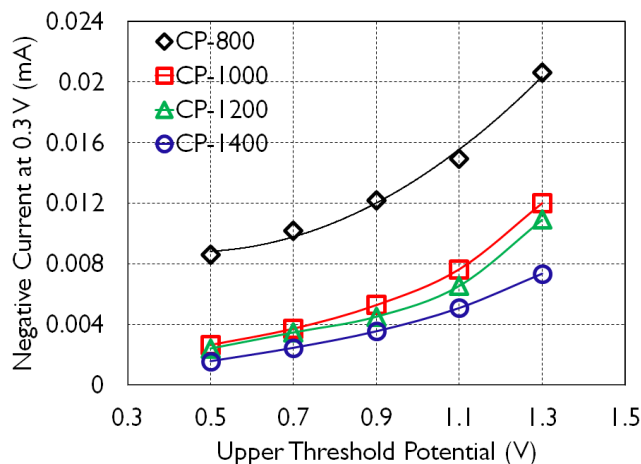


**Figure 5.** Negative currents of the cyclic voltammograms taken at 0.3 V plotted against their upper potential limit for the carbon samples. The data are fitted with a second degree polynomial.

potential was  $< 0.5$  V, confirming that the contribution to the space charge capacitance to the observed capacitance was minimized at approximately 0.3 V for the NOMCs, regardless of their nitrogen content.

Since the minima for all of the NOMCs were at approximately identical potentials, the curvature of the plots in Figure 5 represent the pseudocapacitive behavior of the NOMCs. A consistent decrease in curvature was observed with a decrease in N content. This shows that the pseudocapacitance of the NOMCs systematically decreased with increasing nitrogen content. In the potential range of the experiments, this observation most likely does not speak to the pseudocapacitance of the nitrogen groups, which have a known pseudocapacitance [3, 26, 47-48], but speaks to redox behavior of the oxygen surface groups.

### Helmholtz DL Capacitance

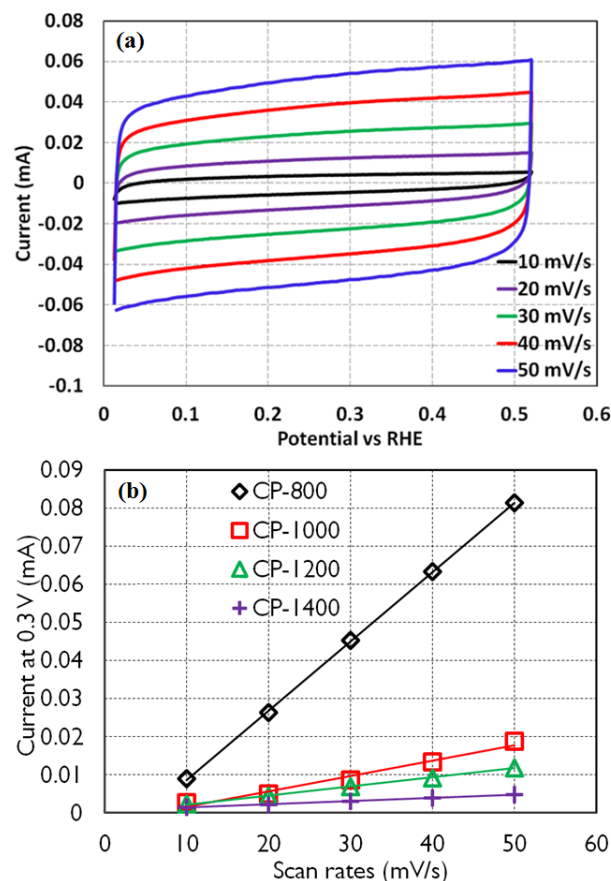
The DL capacitance is typically greatly influenced by surface area, pore size and pore connectivity [39]. However, since the surface area and overall pore structure was identical for all samples, these factors could be ruled out in this work. Since the CP-X carbons were mostly mesoporous, the delay in charge/discharge processes due to microporosity could also be ignored [39]. Additionally, in the CP-X CVs, the transition from positive current to negative current and vice versa at the potential ends were vertical indicating no lag in the charge/discharge rate [49]. Hence, the behavior of DL capacitance found in the NOMCs could be studied on the basis of their surface physicochemical properties, namely basal plane/edge structures and surface chemistry.

Figure 6a shows typical CVs for CP-800 at several scan rates. The CP-X and CS-900 CVs showed a nearly rectangular shape; they were slightly skewed due to IR resistance. The average magnitude of negative and positive currents at the minima observed in Figure 5, 0.3 V, was plotted vs. the scan rate for all of the carbons, which is shown in Figure 6b. Since the data linear,  $C_H$  was obtained from the slopes of the linear plots using Equation 2 [39] and are summarized in Table 4.

$$C_H = \left. \frac{\partial i}{\partial v} \right|_{E=0.3V} \quad (3)$$

where  $i$  is the current,  $v$  is the scan rate.

CS-900 provides a graphitic carbon control with the same pore structure to the NOMCs. The areal capacitance ( $C_{HA}$ ) for CS-900 was  $10.6 \mu\text{F}/\text{cm}^2$ , similar to that of carbon black and activated carbon in the literature [39], validating the data and overall approach. The  $C_{HA}$  of CP-800 was very high,  $25.1 \mu\text{F}/\text{cm}^2$ . The gravimetric capacitance ( $C_{HM}$ ) of CP-800 ( $156.0 \text{ F}/\text{g}$ ) was also high given the relatively low surface area of CP-800 compared with commercial carbons. Among the NOMCs, a gradual increase in both  $C_A$  and  $C_M$  was obtained with an increase in the nitrogen content.



**Figure 6.** (a) Cyclic voltammograms of CP-800 taken at several scan rates in  $N_2$ -saturated  $0.5 \text{ M H}_2\text{SO}_4$  at  $25^\circ\text{C}$ . (b) Dependence of current on the scan rates taken in  $N_2$ -saturated  $0.5 \text{ M H}_2\text{SO}_4$  at  $25^\circ\text{C}$ . The current was obtained by averaging magnitude of current at 0.3 V from the anodic and cathodic scans of the cyclic voltammograms taken at different scan rates.

A traditional and important viewpoint to explain the enhancement in the areal capacitance of the NOMCs is the differences in the microcrystallinity between the carbons. Raman and XRD showed that the length of the graphite domains and stack height were affected by the heat treatment temperature. Differences in  $L_a$  and  $L_c$  have significant implications on the number and ratio between the edge and basal planes; this ratio is important since it is well known that the edge plane has much higher electronic conductivity than the basal plane and, thus, is the dominant surface plane for DL capacitance [48].

From the data in Tables 2 and 3, it was shown that as the temperature treatment increased, the per crystallite basal plane area ( $2 L_a^2$ ) and edge plane area ( $4 L_a L_c$ ) also increased. This led to an edge:basal plane ratio of 0.91 at  $800^\circ\text{C}$  vs 0.81 at  $1400^\circ\text{C}$ . In addition, if the edge area is normalized to the mass per carbon crystallite, the CP-800 sample again has  $\sim 20\%$  more edge area than CP-1400 and  $26\%$  more than CS-900. This result clearly shows that the microcrystallinity differences are insufficient to explain the large increase in  $C_A$ .

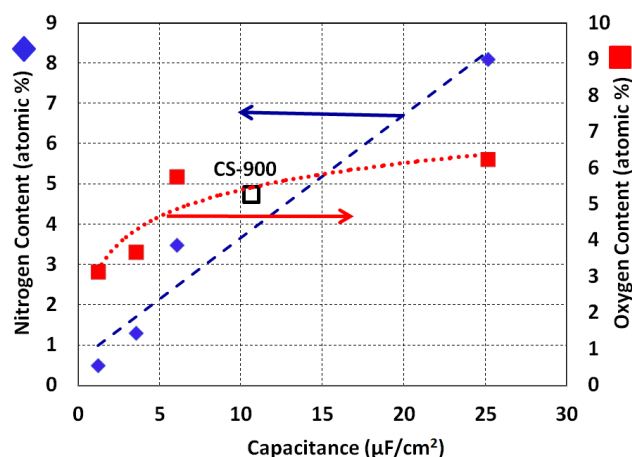


**Figure 7.** The areal capacitance of the carbon samples plotted against their nitrogen (red squares) or oxygen content (blue diamonds). The filled markers represent nitrogen-doped carbons (CP-X) and the empty marker represents non-doped carbon (CS-900). The relationship with nitrogen content is shown with a linear fit and that of oxygen is shown with a logarithmic fit.

Therefore, the only significant differences between the CP-X carbons is their surface composition, which played the most dominant role in dictating the  $C_A$  and  $C_M$ . During XPS, it was observed that both O and N functional groups were present on the carbons. Combining the XPS and CV data, the impact of the N adatom content on  $C_A$  became more clear, and is summarized in the plot in Figure 7. The dependence of  $C_A$  on nitrogen content was fit with a straight line (blue). Although the surface oxygen content also changed with heat treatment, the dependence of  $C_A$  on oxygen content was significantly weaker (red). This suggests that by increasing the nitrogen content, a substantial increase in the  $C_A$  could be achieved within a reasonable range while increasing oxygen content may have little or no effect in DL capacitance above a certain limit. This observation is consistent with other recent work that has shown that capacitance values are more sensitive to nitrogen functional groups than oxygen functional groups [15, 50-54]. This is likely best explained by recent observations by Hulicova et. al [50] who provided a very interesting discussion on electrolyte ion interaction with nitrogen functionalities in acid media. The low charge density of known acidic and alkaline nitrogen functional groups on carbon make them ideal for weak acid/base pairing with electrolyte ions. Not only would this improve electrode wetting, which has been shown experimentally [15], such electrostatic acid/base pairing draws ions from the electrolyte closer to the electrode, shrinking the thickness of the outer Helmholtz plane, increasing the double layer capacity of the electrochemical double layer.

## Conclusions

In this work, NOMCs made from pyrolyzed polypyrrole infiltrated into a SBA-15 template. The N content of the NOMCs was controlled by heat treating to various temperatures between 800-1400 °C while preserving the overall pore

structure of the carbon. Maintaining a constant nanostructure while controlling the surface chemistry of the carbons allowed the contribution of the surface functional groups to be isolated and investigated. After calculating the DL capacitance, it was found that both the specific and gravimetric Helmholtz capacitance increased linearly with the nitrogen content while there was little increase with oxygen content. This was explained by the difference in the acid/base interaction between the N and O functional groups, effectively shrinking the double layer thickness. Therefore, nitrogen functional groups play a greater role in enhancing the DL capacitance of carbon than oxygen functional groups.

## Acknowledgements

The authors would like to thank the U.S. Department of Energy, Office of Basic Energy Sciences under Grant No. DE-FG02-10ER16200 for supporting this work.

## Notes and references

\* Department of Chemical & Biomolecular Engineering, University of Connecticut. Storrs, CT 06269-3222. Email: [mustain@engr.uconn.edu](mailto:mustain@engr.uconn.edu); phone: +1 (860) 486-2756

- 1 B.E. Conway, *J. Electrochem. Soc.*, 1991, **138**, 1539.
- 2 P. Simon, and Y. Gogotsi, *Nat. Mater.*, 2008, **7**, 845.
- 3 D. Hulicova-Jurcakova, M. Seredych, G.Q. Lu and T.J. Bandosz, *Adv. Funct. Mater.*, 2009, **19**, 438.
- 4 Chmiola, J., Yushin, G., Dash, R. K., Hoffman, E. N., Fischer, J. E., Barsoum, M. W. and Gogotsi, Y. *Electrochem. Solid-State Lett.*, 2005, **8**, A357.
- 5 Y. Korenblit, M. Rose, E. Kockrick, L. Borchardt, A. Kvit, S. Kaskel, and G. Yushin, *ACS Nano*, 2010, **4**, 1337.
- 6 D. D. Zhou, Y. -J. Du, Y. -F. Song, Y. -G. Wang, C. -X. Wang, and Y. -Y. Xia, *J. Mater Chem A*, 2013, **1**, 1192.
- 7 K. Jurewicz, K. Babel, A. Ziolkowski and H. Wachowska, *Electrochim. Acta*, 2003, **48**, 1491.
- 8 G. Ciric-Marjanovic, I. Pasti, N. Gavrilov, A. Janosevic, and S. Mentus, *Chemical Papers*, 2013, **67**, 781.
- 9 D. Zhang, X. Zhang, Y. Chen, P. Yu, C. Wang and Y. Ma, *J. Power Sources*, 2011, **196**, 5990
- 10 R.K. Sharma, A.C. Rastogi, and S.B. Desu, *Electrochem. Commun.*, 2008, **10**, 268.
- 11 K. Jurewicz, S. Delpoux, V. Bertagna, F. Beguin, and E. Frackowiak, *Chem. Phys. Lett.*, 2001, **347**, 36.
- 12 H. Chang, C. Chang, Y. Tsai, and C. Liao, *Carbon*, 2012, **50**, 2331.
- 13 G. Lota, B. Grzyb, H. Machnikowska, J. Machnikowski, and E. Frackowiak, *Chem. Phys. Lett.*, 2005, **404**, 53.
- 14 C. Shen, Y. Sun, W. Yao, and Y. Lu, *Polymer*, 2014, **55**, 2817.
- 15 S.L. Candelaria, B.B. Garcia, D. Liu, and G. Cao, *J. Mater. Chem.*, 2012, **22**, 9884.

- 16 D. Mang, H. P. Boehm, K. Stanczyk and H. Marsh, *Carbon*, 1992, **30**, 391.
- 17 S. Maldonado and K. J. Stevenson, *J. Phys. Chem. B*, 2005, **109**, 4707.
- 18 Y. Shao, G. Yin and Y. Gao, *J. Power Sources*, 2007, **171**, 558.
- 19 S. Shrestha and W. E. Mustain, *J. Electrochem. Soc.*, 2010, **157**, B1665.
- 20 M. Inagaki, H. Konno and O. Tanaike, *J. Power Sources*, 2010, **195**, 7880.
- 21 Y. Zhai, Y. Dou, D. Zhao, P. F. Fulvio, R. T. Mayes and S. Dai, *Adv. Mater.*, 2011, **23**, 4828.
- 22 F. Béguin, K. Szostak, G. Lota, and E. Frackowiak, *Adv. Mater.*, 2005, **17**, 2380.
- 23 D.W. Wang, F. Li, L. -C. Yin, X. Lu, Z. -G. Chen, I. R. Gentle, G. Q. Lu, and H. -M. Cheng, *Chem. Eur. J.*, 2012, **18**, 5345.
- 24 D.W. Wang, F. Li, Z. -S. Wu, W. Ren, and H. -M. Cheng, *Electrochem. Commun.*, 2009, **11**, 1729.
- 25 L. L. Zhang, X. Zhao, H. Ji, M. D. Stoller, L. Lai, S. Murali, S. McDonnell, B. Cleveger, R. M. Wallace and R. S. Ruoff, *Energy Environ. Sci.*, 2012, **5**, 9618.
- 26 J.D. Wiggins-Camacho and K.J. Stevenson, *J. Phys. Chem. C*, 2009, **113**, 19082.
- 27 D. Zhao, J. Feng, Q. Huo, N. Melosh, G. H. Fredrickson, B. F. Chmelka and G. D. Stucky, *Science*, 1998, **279**, 548.
- 28 R. Ryoo, S. H. Joo, and S. Jun, *J. Phys. Chem. B*, 1999, **103**, 7743.
- 29 H. Yang, Y. Yan, Y. Liu, F. Zhang, R. Zhang, Y. Meng and M. Li, *J. Phys. Chem. B.*, 2004, **108**, 17320.
- 30 C. M. Yang, C. Weidenthaler, B. Spliethoff, M. Mayanna and F. Schüth, *Chem. Mater.*, 2005, **17**, 355.
- 31 A. B. Fuertes and T. A. Centeno, *J. Mater. Chem.*, 2005, **15**, 1079.
- 32 H. I. Lee, J. H. Kim, D. J. You, J. E. Lee, J. M. Kim, W. -S. Ahn, C. Pak, S. H. Joo, H. Chang and D. Seung, *Adv. Mater.*, 2008, **20**, 757.
- 33 M. Kruk, M. Jaroniec, Y. Sakamoto, O. Terasaki, R. Ryoo and C. H. Ko, *J. Phys. Chem. B*, 2000, **104**, 292.
- 34 M. Kruk, M. Jaroniec and A. Sayari, *Langmuir*, 1997, **13**, 6267.
- 35 M. De Graff and M. E. McHenry, *Structure of Materials: An Introduction to crystallography, Diffraction, and Symmetry*, p. 318, Cambridge University Press, New York (2007).
- 36 M. Kruk, M. Jaroniec, C. H. Ko and R. Ryoo, *Chem. Mater.*, 2000, **12**, 1961.
- 37 A. B. Fuertes and D. M. Nevskaja, *Microporous Mesoporous Mater.*, 2003, **62**, 177.
- 38 A. B. Fuertes and T. A. Centeno, *J. Mater. Chem.*, 2005, **15**, 1079.
- 39 K. Kinoshita, *Carbon: Electrochemical and Physicochemical Properties*, John Wiley & Sons, New York (1988).
- 40 A. C. Ferrari and J. Robertson, *Phys. Rev. B*, 2000, **61**, 14095.
- 41 D. S. Knight and W. B. White, *J. Mater. Res.*, 1989, **4**, 385.
- 42 F. Tuinstra and J. L. Koenig, *J. Chem. Phys.*, 1970, **53**, 1126.
- 43 T. Jawhari, A. Roid and J. Casado, *Carbon*, 1995, **33**, 1561.
- 44 M. S. Dresselhaus, A. Jorio, M. Hofmann, G. Dresselhaus and R. Saito, *Nano. Lett.*, 2010, **10**, 751.
- 45 H. Sjöström, S. Stafström, M. Boman and J. E. Sundgren, *Phys. Rev. Lett.*, 1995, **75**, 1336.
- 46 Z. Q. Li, C. J. Lu, Z. P. Xia, Y. Zhou and Z. Luo, *Carbon*, 2007, **45**, 1686.
- 47 N.D. Kim, W. Kim, J.B. Joo, S. Oh, P. Kim, Y. Kim and J. Yi, *J. Power Sources*, 2008, **180**, 671.
- 48 D. Hulicova, M. Kodama and H. Hatori, *Chem. Mater.*, 2006, **18**, 2318.
- 49 E. Frackowiak and F. Béguin, *Carbon*, 2001, **39**, 937.
- 50 Y.H. Lee, K. Chang and C. Hu, *J. Power Sources*, 2013, **227**, 300.
- 51 H.M. Jeong, J.W. Lee, W.H. Shin, Y.J. Choi, H.J. Shin, J.K. Kang and J.W. Choi, *Nano Letters*, 2011, **11**, 2472.
- 52 M. Galinski, K. Babel and K. Jurewicz, *J. Power Sources*, 2013, **228**, 83.
- 53 L. Wei, M. Sevilla and A.B. Fuertes, *Adv. Func. Mat.*, 2012, **22**, 827.
- 54 Z. Zapata-Benabithé, F. Carrasco-Marin and C. Moreno-Castilla, *J. Power Sources*, 2012, **219**, 80.